



OPEN ACCESS

EDITED BY

Jose Luis Iriarte,
Austral University of Chile, Chile

REVIEWED BY

July Andrea Corredor Acosta,
University of Concepción, Chile
Francisco Werner,
National Marine Fisheries Service
(NOAA), United States

*CORRESPONDENCE

Xiaojun Yan
yanxj@zjou.edu.cn

SPECIALTY SECTION

This article was submitted to
Marine Fisheries, Aquaculture and
Living Resources,
a section of the journal
Frontiers in Marine Science

RECEIVED 18 August 2022

ACCEPTED 26 September 2022

PUBLISHED 11 October 2022

CITATION

Cai L, Tang R, Yan X, Zhou Y, Jiang J
and Yu M (2022) The spatial-temporal
consistency of chlorophyll-a and
fishery resources in the water of the
Zhoushan archipelago revealed by
high resolution remote sensing.
Front. Mar. Sci. 9:1022375.
doi: 10.3389/fmars.2022.1022375

COPYRIGHT

© 2022 Cai, Tang, Yan, Zhou, Jiang and
Yu. This is an open-access article
distributed under the terms of the
[Creative Commons Attribution License
\(CC BY\)](https://creativecommons.org/licenses/by/4.0/). The use, distribution or
reproduction in other forums is
permitted, provided the original
author(s) and the copyright owner(s)
are credited and that the original
publication in this journal is cited, in
accordance with accepted academic
practice. No use, distribution or
reproduction is permitted which does
not comply with these terms.

The spatial-temporal consistency of chlorophyll-a and fishery resources in the water of the Zhoushan archipelago revealed by high resolution remote sensing

Lina Cai^{1,2}, Rong Tang¹, Xiaojun Yan^{1*}, Yongdong Zhou³,
Jingjing Jiang¹ and Menghan Yu¹

¹Marine Science and Technology College, Zhejiang Ocean University, Zhoushan, China, ²Donghai Laboratory, Zhoushan, Zhejiang, China, ³Zhejiang Marine Fisheries Research Institute, Zhejiang Ocean University, Zhoushan, China

Details of the chlorophyll-a (Chl-a) distribution in the water of the Zhoushan archipelago were analyzed based on data from the panchromatic multispectral sensor (PMS) of the GaoFen-6 (GF-6). A new Chl-a inversion model was built using *in-situ* Chl-a and the green-red bands of the 2 m spatial resolution GF-6/PMS image. Combined with fishery data, the relationship between Chl-a concentration and fish resources were revealed. The results show that: (1) High Chl-a concentration area was mainly concentrated in the nearshore intensive islands waters, and Chl-a concentration changes obviously with the change of tidal currents. Chl-a concentration around islands increases, especially downstream of islands. Seasonally, Chl-a concentration is higher in spring and summer, lower in autumn, and lowest in winter. (2) The change of fish eggs and larvae in the water of the Zhoushan archipelago shows consistency with the spatial distribution and seasonal variation of Chl-a. (3) The interaction between tidal currents and islands results in the diverse currents (upstream upwelling and downstream vortex currents) around the islands, promoting vertical water exchange and the uplifting of nutrients, resulting in a high overall Chl-a concentration in the waters around the islands. The diverse flow conditions, the ideal nutrient-rich environment, and the abundant phytoplankton attract a large number of fish to gather and breed in the waters around the islands. (4) Chl-a of intensive island waters is an essential indicator for fish spawning grounds.

KEYWORDS

Gaofen-6, chlorophyll a, fish egg, larvae, Zhoushan archipelago

1 Introduction

Zhoushan fishing ground is located at the mouth of the Yangtze River and Hangzhou Bay. The superior geographical location and the unique ecological conditions of the Zhoushan fishing ground provide sufficient bait and living space for various marine organisms, forming the largest excellent fishing ground in China (Chang et al., 2012). The Zhoushan Archipelago is dotted with hundreds of islands, which becomes a good spawning and baiting ground for many kinds of economic fishes, as well as a necessary route for marine organisms to anadromous rivers and descend to the sea (Liang et al., 2020). Those superior geographical conditions for Zhoushan fishing ground support its fishery ecosystems as the ideal place of spawning and feeding for numerous fish species, and has been established as the most important fishing ground in China with the highest catching yield. However, the precise description of the environmental conditions for this place, especially the interrelationships between the spatial-temporal distribution of high-resolution chlorophyll-*a* (Chl-*a*) and fishery resources is lacking mostly owing to the highly intensive nearshore islands and high contents of suspended substances, namely, the muddy waters. Therefore, the improvement of remote sensing method is necessary for its application to characterize the above scientific question.

With the appearance of traditional satellite data and the increase in data sources, satellite remote sensing has become widely used for fishery analysis. Many environmental factors including sea surface temperature (SST) (Habibullah et al., 2020), Chl-*a* concentration (Paulino et al., 2016), primary productivity (Lee et al., 2015), ocean front boundaries (Xu et al., 2017), currents and water masses (Sun et al., 2013) and other marine environmental parameters (Kourti et al., 2001; Barbieri et al., 2004), can be obtained from satellite data. Based on these environmental factors, the distribution of fish stocks can be better grasped, and the prediction of the direction of fishery movement can be realized, which reduces the time for fishermen to find fishing grounds.

Chl-*a* is the main photosynthetic pigment of marine phytoplankton as well as an indicator of phytoplankton biomass, which can indicate the basic state of the aquatic food chain (Bierman et al., 2011). It is the basis of geochemical cycles in the world ocean and a basic indicator for estimating marine productivity, as well as a basic basis for judging the fertility of waters and evaluating the potential productivity of fisheries in waters (Bacher et al., 2003; Huot et al., 2007). In addition, the variation and distribution of Chl-*a* content are closely related to SST, nutrient salinity, currents, and upwelling (Richardson et al., 2005).

Based on satellite, many methods have been applied to detect Chl-*a* concentration in class II water. For example, in the study of Canadian nearshore waters using the Moderate Resolution

Imaging Spectroradiometer (MODIS) sensor, it was found that the effect of turbid water on Chl-*a* concentration is based on a foundation that the influence of turbidity water on Chl-*a* estimation can be attenuated by modifying the absorption characteristics of Colored Dissolved Organic Matter (CDOM) in the GSM01 algorithm (Tilstone et al., 2011). Chl-*a* in nearshore waters of the Yangtze River estuary in China retrieved from Medium Resolution Imaging Spectrometer (MERIS) improved the estimation of Chl-*a* concentration in turbid water using the new indicator SCI algorithm. (Shen et al., 2010). Algorithms for Chl-*a* inversion in turbid nearshore waters were established using Sea-viewing Wide Field-of-view Sensor (SeaWiFS) data (Dall'Olmo et al., 2005) to convert blue-green reflectance ratios to near-infrared and red-light ratios. Landsat's Thematic Mapper (TM) (Duan et al., 2007; Nazeer and Nichol, 2016), Enhanced Thematic Mapper Plus (ETM+) (Tebbs et al., 2013; Nazeer and Nichol, 2016), and Operational Land Imager (OLI) (Kim et al., 2016; Fu et al., 2018) sensors have also been applied to analyze Chl-*a* in class II water.

However, limited by the low resolution of these satellite data and the lack of nearshore data, the refined research on nearshore turbid waters and island-reef intensive fisheries are relatively lacking.

With the advantages of high spatial resolution, high spectral resolution and high temporal resolution, multiple data sources, and easy access, GF series satellites have become an effective supplement to remote sensing satellite data sources in the study of inland water environment and small-scale nearshore water quality monitoring (Cai et al., 2020; Zhai et al., 2021).

GaoFen-6 satellite (GF-6) is a low-orbiting optical remote sensing satellite that is equipped with a panchromatic and multispectral sensor (PMS) and a wide field-of-view (WFV) sensor. The PMS sensor has a high resolution of 2 m, which can be well applied to the observation of small-scale features (Wang et al., 2021).

Zhoushan archipelago fishing ground is characterized by thousands of intensive nearshore islands with small spatial scales (from several kilometers to several meters, or even sub-meter level) and complex shapes (Fu et al., 2019). However, the precise description of the environmental conditions for this place, especially the interrelationships between the spatial-temporal distribution of high-resolution Chl-*a* and fishery resources, is still lacking. We need to combine the perspectives of high spatial resolution (from meter level to sub-meter level) and high temporal resolution satellite observation to carry out research, and there is an urgent need to develop new algorithms for high-resolution Chl-*a*.

This paper developed a new Chl-*a* algorithm based on high resolution (2 m) GF-6/PMS data and analyzed the spatial variation of Chl-*a* in the water of the Zhoushan archipelago. Combined with the measured fishery data in 2014 and 2015 and many other data, we revealed the close correlation between Chl-*a* and the variation

of fishery resources. This paper provides scientific support for the development of nearshore islands type of fisheries.

2 Material and method

2.1 Study area

The Zhoushan archipelago ($121^{\circ}30'E$ - $123^{\circ}25'E$, $29^{\circ}32'N$ - $31^{\circ}04'N$) is located in the shallow sea area of the continental shelf in the northwestern part of the East China Sea, with many offshore islands and a winding coastline. It is the largest archipelago in China with 4 696 islands, with a total area of $22\,200\text{ km}^2$, including $20\,800\text{ km}^2$ sea area and $1\,440.2$ land area. The Zhoushan fishing ground is located at the southern mouth of Hangzhou Bay, adjacent to the confluence of the Changjiang Diluted Water, the Qiantang River's water, and the East China Sea, and is characterized by strong tides, which are controlled by semidiurnal tides (Chen et al., 1990).

The detailed information about the study area ($121^{\circ}48'E$ - $123^{\circ}00'E$, $29^{\circ}36'N$ - $31^{\circ}00'N$) was shown in Figure 1.

2.2 Satellite data

The GF-6 satellite, launched on June 2, 2018, is a low-orbit optical remote sensing satellite and the first Chinese GaoFen satellite for agricultural observation. The satellite is loaded with a

2 m panchromatic band, 8 m multispectral high-resolution PMS sensor, and 16 m multispectral medium-resolution WFV sensor (Table 1). The PMS sensor carried by GF-6 has the widest observation width among satellites with 2 m resolution, up to 95 km. The satellite adds the “red edge” band and ultraviolet band to the WFV sensor, and the observation width reaches 800 km. This has played an important role in effectively reflecting the specific spectral characteristics of crops, natural resource investigation and monitoring, disaster prevention and mitigation (Deng et al., 2021; Xia et al., 2022). GF-6/PMS images of L1A from 2019 to 2021 used in this study are from the China Ocean Satellite Data Service (<https://osdds.nsoas.org.cn/>).

In addition, Landsat-8 satellite remote sensing images (<http://www.gscloud.cn/>) were applied as supplementary in this study. Landsat-8 contains both Operational Land Imager (OLI) and Thermal Infrared Sensor (TIRS) sensors with a replay period of 16 d. The OLI sensor includes 9 bands, with a spatial resolution of 30 m for B1-B7 and B9, and 15 m for B8 (Table 2). In this paper, the L1T-level product data of Landsat-8/OLI with geometric refinement correction taken in 2014 and 2015 in the Zhoushan Archipelago Sea area were selected.

2.3 In situ data

2.3.1 Measured data of Chl-a

A comprehensive operational survey was conducted in the water of the Zhoushan archipelago from 24 to 31 October

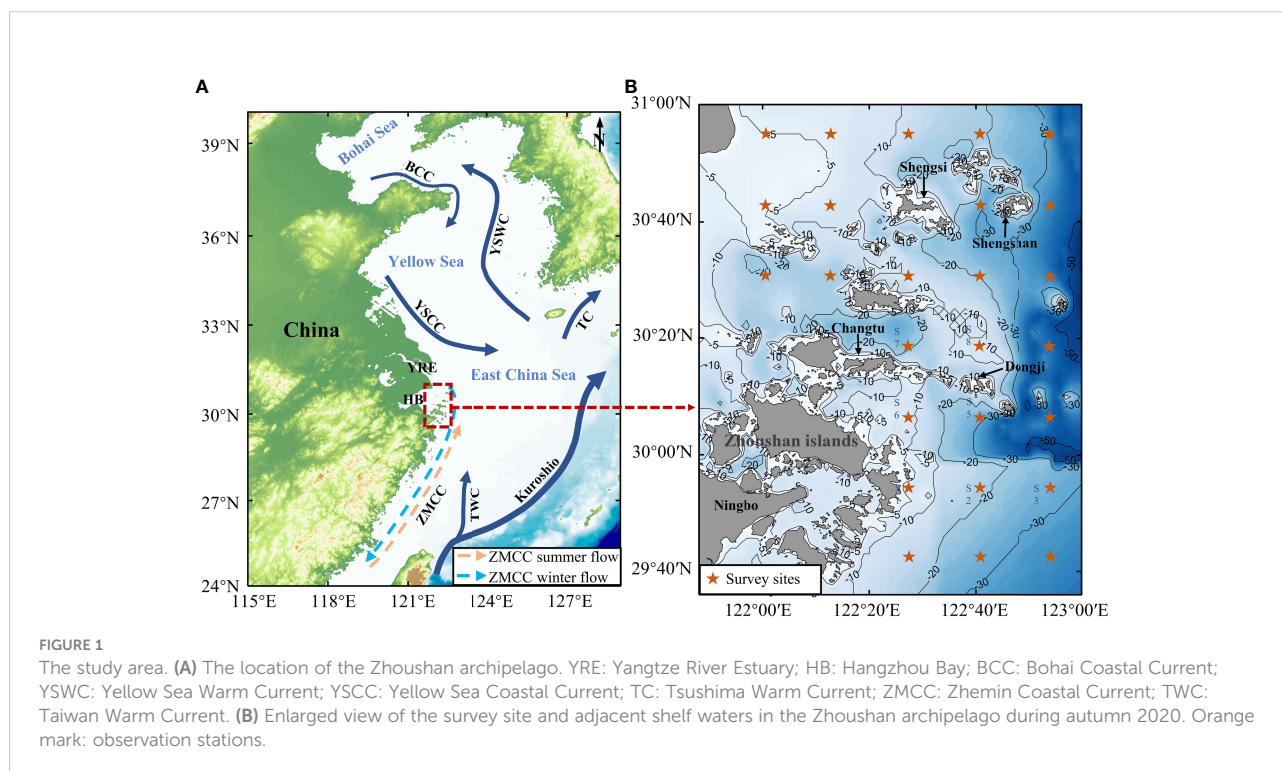


TABLE 1 Information of GF-6 PMS and WFV.

Sensor	Band No.	Spectral range (μm)	Spatial resolution (m)	Width (km)	Repetition cycle (d)
PMS	B1(Blue)	0.45-0.52	8	≥ 90	41
	B2(Green)	0.52-0.60			
	B3(Red)	0.63-0.69			
	B4(NIR)	0.77-0.89			
	B5(Pan)	0.45-0.90			
WFV	B1(Blue)	0.45-0.52	16	≥ 800	4
	B2(Green)	0.52-0.59			
	B3(Red)	0.63-0.69			
	B4(NIR)	0.77-0.89			
	B5(Coastal)	0.40-0.45			
	B6(Yellow)	0.59-0.63			
	B7(RedEdge1)	0.69-0.73			
	B8(RedEdge2)	0.73-0.77			

NIR, Near-Infrared; Pan, Panchromatic band.

2020. Totally, 148 valid Chl-*a* concentration field sampling observations were collected (Figure 1B). The samples were divided randomly into two groups, including the modeling group and testing group, with samples of 88 and 60, respectively.

The Chl-*a* concentration was measured spectrophotometrically (Jeffrey and Humphrey, 1975) in this study using 90% acetone (Ritchie, 2018) as the solvent. The specific procedure of the measurement is as follows. Water samples were taken from the surface layer at a depth of 5 m, with a filtered volume of 500 ml of seawater. The water samples were filtered and cryopreserved. The filter membrane containing the Chl-*a* sample was folded in half into a centrifuge tube, and extracted Chl-*a* with a 90% acetone solution for 16-24 h at low temperature, protecting from light. After the extraction, Chl-*a* standard solution was measured using the TU1810D UV-V spectrophotometer. Meanwhile, its absorbance values at 750 nm, 664 nm, 647 nm, and 630 nm were obtained. The absorbance of the sample was corrected by using 90% acetone as a blank absorbance measurement. Chl-*a* concentration of the extract

was obtained using Eq. (1).

$$P_1 = 11.85(A_{664} - A_{750}) - 1.54(A_{647} - A_{750}) - 0.08(A_{630} - A_{750}) \quad (1)$$

Where P_1 is the mass concentration of Chl-*a* in the extract; A^i is the absorbance of the extract at wavelength i nm.

Subsequently, Chl-*a* concentration in the water samples were calculated using Eq. (2).

$$P = P_1 * V_1 / V_\delta \quad (2)$$

Where P is the mass concentration of Chl-*a* in the water sample; P_1 is the mass Chl-*a* concentration in the extraction solution; V is the volume of the water sample; V_1 is the constant volume of the extraction solution; δ is the optical range of the cuvette.

Eq. (1) and (2) refer to the determination criteria in Water Quality - Determination of Chlorophyll *a* - Spectrophotometric Method (HJ897-2017) (https://www.mee.gov.cn/ywqgz/fgbz/bz/bzwb/jcffbz/201712/t20171227_428728.shtml).

TABLE 2 Information of Landsat-8 OLI.

Sensor	Band No.	Spectral range (μm)	Spatial resolution (m)	Width (km)	Repetition cycle (d)	
OLI	B1(Coastal)	0.433-0.453	30	185	16	
	B2(Blue)	0.450-0.515				
	B3(Green)	0.525-0.600				
	B4(Red)	0.630-0.680				
	B5(NIR)	0.845-0.885				
	B6(SWIR 1)	1.560-1.660				
	B7(SWIR 2)	2.100-2.300				
	B8(Pan)	0.500-0.680				15
	B9(Cirrus)	1.360-1.390				30

2.3.2 Fishery data

The measured data on the total number of fish eggs and larvae in the water of the Zhoushan archipelago was obtained from the fishery resources and ecological environment surveys conducted by the Zhejiang Institute of Marine Fisheries on 11 cruises in 2013, 2014, and 2015 on the nearshore waters of northern Zhejiang. Based on actual fishery measurements of the total number of fish eggs and larvae in March, May, July, November 2014, April, and August 2015, the corresponding spatial and temporal distribution of fish eggs and larvae was analyzed in this study. The distribution of the spawning and baiting grounds of silver pomfret, Japanese anchovy, croaker, and cuttlefish, in the Zhoushan fishing ground, was obtained from the data of the distribution of the three grounds and one channel of the main economic species in the East China Sea area (Zhou and Li, 2018).

2.4 SST, SSS, wind field, currents and topography data

In this paper, GF-6/PMS satellite data (2019–2021) and Landsat-8/OLI satellite data (2014–2015) were selected to analyze the seasonal change of Chl-*a* concentration in the waters of Zhoushan archipelago and the Chl-*a* change details near islands. Fishery data (2014–2015) was analyzed to reveal the general distribution of fish eggs and larvae in the waters of the Zhoushan archipelago. The MUR-SST (°C) data, SSS (‰) data, Wind data, Ocean current (m/s) data, and Topography (m) data (Table 3) are applied to show the background information of the study area, including the hydrological environment, topography, and hydrodynamic conditions. All these data and methods combined together to reveal the relationship between fishery resources and the environmental factors Chl-*a* concentration, for example). Meanwhile, these materials and methods can also help us analyze the reasons contributing to the change of Chl-*a* and fishery resources.

The sources of oceanic and atmospheric data and relevant information were shown in Table 3.

2.5 Data processing

The preprocessing of 18 GF-6/PMS multispectral images, including radiometric calibration, atmospheric correction, orthorectification, image fusion, and water extraction, was performed with ENVI 5.3 to improve image quality and usability (Pan et al., 2021).

The radiometric calibration uses the GF-6/PMS image calibration coefficients (Table 4) provided by the China Resources Satellite Application Center (<http://www.cresda.com>) to convert the Digital Number (DN) recorded in the original settings of the image into reflectance information of the outer surface of the atmosphere (Yang et al., 2020). The calibration equation uses Eq. (3).

$$L_{\lambda} = Gain * DN + Bias \quad (3)$$

Where L_{λ} is the spectral radiation at the sensor entrance pupil, *Gain* is the gain value, *Bias* is the offset value, and *DN* is the Digital Number.

The Fast Line-of-Sight Atmospheric Analysis of Spectral Hypercubes (FLAASH) module was used in this study to perform atmospheric correction of the calibrated Top of Atmosphere reflectance to eliminate the errors caused by the atmosphere during its scattering, absorption, and reflection (Perkins et al., 2005).

The orthorectification correction eliminates the effects of terrain and distortions caused by camera orientation. The study used the Rational Polynomial Coefficients (RPC) geometry correction module to orthorectify the panchromatic and multispectral images of GF-6/PMS using GMTED2010 (The Global Multi-resolution Terrain Elevation Data 2010) data as a reference (Gianinetto and Scaioni, 2008).

Image fusion was performed using the Nearest Neighbor Diffusion (NNDiffuse) Pan Sharpening fusion algorithm, which resulted in good retention of image color, texture features, and spectral information. The fused images have a resolution of 2 m to facilitate subsequent image analysis studies (Wang et al., 2021).

In order to eliminate the influence of land on water information in the image, according to the characteristics of

TABLE 3 Data sources and related information.

Field (units)	Data source	Spatiotemporal resolution	Reference
MUR-SST (°C)	NASA JPL PO. DAAC	1 km/1 d	https://registry.opendata.aws/mur/
SSS (‰)	GLOBAL_ANALYSIS_FORECAST_PHY_001_024	0.083°/1 month	https://doi.org/10.48670/moi-00016
10m wind (m/s)	NOAA/NCEP GFS Atmospheric Model	0.5°/3 h	http://pacioos.org/metadata/ncep_global.html
Ocean current (m/s)	FVCOM	1 km/1 h	(Chen et al., 2006)
Topography (m)	NOAA/NGDC ETOPO1	1 arc-min	http://www.ngdc.noaa.gov/mgg/global/global.html

MUR-SST, Multi-Scale Ultra High Resolution-Sea Surface Temperature; SSS, Sea Surface Salinity; GLOBAL_ANALYSIS_FORECAST_PHY_001_024, Global Ocean Sea Physical Analysis and Forecasting Products; NOAA/NCEP, National Oceanic and Atmospheric Administration/National Centers for Environmental Prediction; GFS, Global Forecast System; FVCOM, Finite-Volume, primitive equation Community Ocean Model; PO. DAAC, Physical Oceanography Distributed Active Archive Center; GEBCO, General bathymetric chart of the oceans; NGDC, National Geophysical Data Center.

TABLE 4 GF-6 PMS calibration parameters in 2019.

Satellite payloads	Band No.	Gain	Bias
PMS	B1	0.0847	0
	B2	0.0653	
	B3	0.0491	
	B4	0.0289	
	B5	0.0534	

the vast difference between ocean and land reflection spectra, the Normalized Difference Water Index (NDWI) was calculated using the B4 and B2 of GF-6/PMS. The threshold of NDWI was set to achieve water extraction in the nearshore water (Jawak and Luis, 2015).

Significant differences exist in shape and spectral range of the spectral response function curves for each band of GF-6/PMS and Landsat8/OLI. In addition, GF-6/PMS and Landsat-8/OLI differ in altitude, orbit, inclination, and spatial resolution. These factors can have an impact on the observation value of each sensor.

GF-6/PMS data were not available for the period from 2014 to 2015, as a supplement, Landsat-8/OLI images were utilized, and Chl-*a* was analyzed using the model from previous studies (Huang et al., 2016). The formula is as follows:

$$\rho = 124.3*(B4)^2 + 15.28*(B4) + 0.914 \quad (4)$$

Where ρ is Chl-*a* concentration, and B4 is red band reflectance in Landsat-8 image.

3 Result

3.1 Establishment of Chl-*a* inversion model

Based on fitted GF-6/PMS spectral data of each channel and the measured Chl-*a* concentration data, Chl-*a* inversion models were constructed using the waveband combination, and the best applicable model was applied to inverse Chl-*a* using the GF-6/PMS remote sensing images.

In order to ensure the reliability of the model, we establish the inversion model using as much data as possible. Therefore, the amount of data is critical, and more data were applied to build the model. As for the percentage, it doesn't matter how big or how little the percentage is, as long as we can ensure the amount of data for modeling and validation. In prior studies, 20-80 *in-situ* data were also used to build and to verify a model (Nazeer and Nichol, 2016; Cai et al., 2020).

From 148 measured data samples, we selected 88 for inversion model construction and 60 for model validation.

3.1.1 Sensitive bands and band combinations for Chl-*a*

The spectral features of chlorophyll are the main basis for Chl-*a* concentration information extraction (Lin et al., 2016). Therefore, the concentration of Chl-*a* can be estimated based on the different wavelength reflectance. The sensitivity between Chl-*a* concentration and reflectance in the B1-B4 band of GF-6/PMS images was analyzed. The model accuracy was assessed using the root mean square error (RMSE) (Eq. (5)).

$$RMSE = \sqrt{\frac{1}{n} \sum_{i=1}^n (Chl-a_i^{estimated} - Chl-a_i^{measured})^2} \quad (5)$$

Where $Chl-a_i^{estimated}$ is the model estimate value, $Chl-a_i^{measured}$ is the field measurement value, and n is the number of sample points.

The correlation between the B1, B2, and Ln (Chl-*a*) (natural logarithm of Chl-*a*) was low and negative, with the coefficient of determination of 0.3786 and 0.4860, respectively (Figures 2A, B). The B3 and B4 were positively correlated with Ln (Chl-*a*) with R^2 of 0.6356 and 0.8172 (Figures 2C, D), indicating that the B4 (NIR) was the most sensitive to Chl-*a* concentration.

Suspended Sediment Concentration (SSC) in the Zhoushan Archipelago Sea area is generally at a high level, up to 1.103 g/L, mainly distributed west of 122.3°E (Cai et al., 2020). In order to reduce the interference of SSC on the spectral characteristics of the Chl-*a* inversion process and effectively extract the concentration information of Chl-*a*, B4 (NIR) is not considered in this band combination modelling process.

Some Chl-*a* inverse models were obtained by combining different bands in prior studies using low spatial resolution satellite data (Le et al., 2009; Moses et al., 2009). Moreover, the combination of multiple bands can effectively eliminate the influence of water bodies and related environmental changes to a certain extent (Chen et al., 2013). This study tried to combine B1, B2, and B3 to establish the Chl-*a* inverse algorithm. Totally 63 multi-band combinations were listed, from which 26 band combinations with a high correlation with Chl-*a* concentration ($R^2 > 0.45$) were selected for analysis (Table 5).

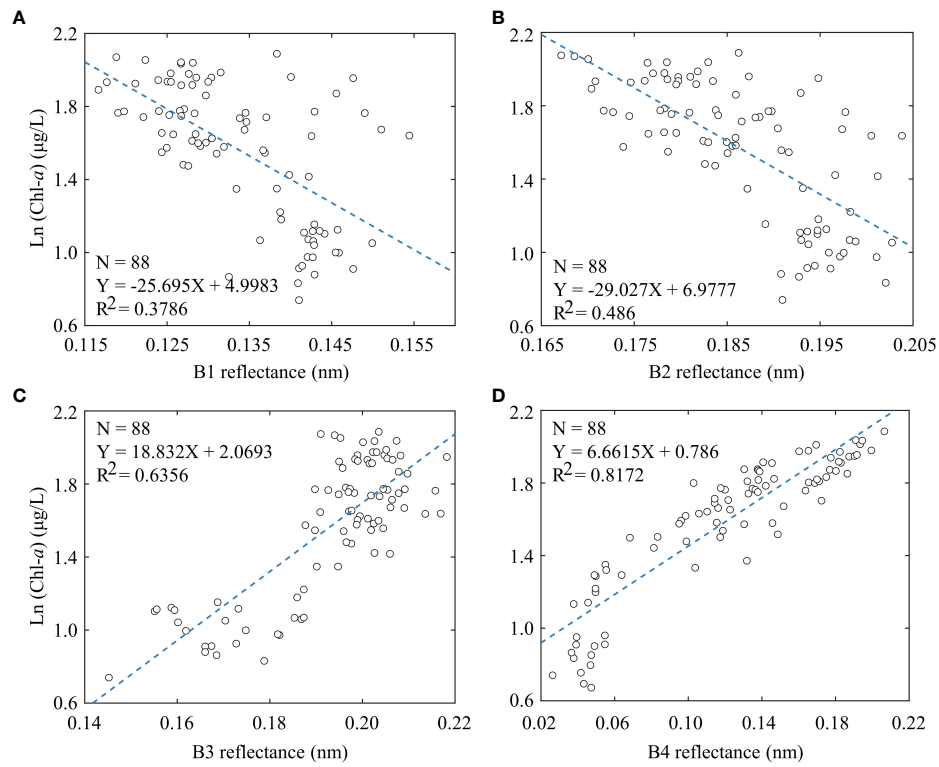


FIGURE 2
 Correlation between the band value retrieved from PMS image after atmosphere correction and sampled Chl-a. (A–D): The linear relationship between the reflectance of band 1, 2, 3, 4 and Chl-a concentration. The abscissa is the reflectance of a single band, and the ordinate is the natural logarithm of Chl-a [Ln (Chl-a)].

3.1.2 Model building

Six multispectral band combination models $(B2 - B3)/(B2 + B3)$, $B1 * B2/B3$, $B2/B3 + B1$, $B3/(B1 + B2)$, $B3/B2$ and $B3 - B2$ with $R^2 > 0.75$ are selected from Table 5 for regression analysis and interpretation.

Using linear, power, and exponential functions as fitting functions (Le et al., 2013; Cai et al., 2020), the model expressions between each band combination and the measured Chl-a concentration data were constructed, and a total of 20 models were analyzed (Table 6).

TABLE 5 Band combination.

Band combination (X)	R ²	Band combination (X)	R ²
$(B2 - B3)/(B2 + B3)$	0.7997	$B2/B1 + B3$	0.5487
$(B1 - B3)/(B1 + B3)$	0.6890	$B3/B1 + B2$	0.6997
$(B1 - B3)/B2$	0.7378	$B3/(B1 + B2)$	0.7766
$(B2 - B3)/B1$	0.7060	$B2/(B1 + B3)$	0.7426
$(B1 - B2)/B3$	0.6386	$B1/(B2 + B3)$	0.5981
$B1 * B2 - B3$	0.6422	$B3/(B1 - B2)$	0.5975
$B1 * B2/B3$	0.7676	$B2/(B1 - B3)$	0.5209
$B1 * B3/B2$	0.4567	$B1/(B2 - B3)$	0.4968
$B2 * B3/B1$	0.5278	$B3/B1$	0.7089
$B2/B3 + B1$	0.7808	$B3/B2$	0.8273
$B1/B3 + B2$	0.6889	$B2/B1$	0.6857
$B3/B2 + B1$	0.7273	$B3 - B2$	0.8194
$B1/B2 + B3$	0.5762	$B3 - B1$	0.6894

The correlation analysis in Table 6, shows that the model established by the power exponential function of the ratio of B2 and B3 provides the best accuracy ($R^2 = 0.8901$, $RMSE = 0.1260$ $\mu\text{g/L}$). Therefore, this model (named PMS-Chla) (Eq. (6) and Eq. (7)) is suitable for retrieving Chl-*a* concentration in the nearshore waters of the Zhoushan archipelago using GF-6/PMS data.

$$X = Rrs(B3)/Rrs(B2) \quad (6)$$

$$\rho = \exp(1.401X^{2.423}) \quad (7)$$

here ρ is the Chl-*a* concentration in $\mu\text{g/L}$, $Rrs(B2)$ and $Rrs(B3)$ are the reflectance of PMS data in green and red bands, respectively.

Comparing the modelled data and *in-situ* value (Zawadzki and Kedzior, 2016) is necessary. The modelled Chl-*a* in Figures 3A, B were acquired simultaneously with the *in-situ* data. The results show that the new model (PMS-Chla) based on GF-6/PMS data can be used to invert the Chl-*a* concentration in the waters of the Zhoushan area with R^2 of 0.9065 and $RMSE$ of 0.5377 $\mu\text{g/L}$ (Figure 3A). The model Chl-*a* values based on the Landsat8/OLI model and the *in-situ* Chl-*a* values showed good validation results with R^2 of 0.8338 and $RMSE$ of 0.6284 $\mu\text{g/L}$ (Figure 3B).

3.2 Chl-*a* distribution in Zhoushan archipelago area

Chl-*a* distribution details in the Zhoushan archipelago area from 2019 to 2021 were analyzed based on the newly built model (PMS-Chla). Meanwhile, as a supplement, Landsat-8/OLI images from 2014 to 2015 were utilized, and Chl-*a* was analyzed using the model from previous studies (Huang et al., 2016). The Chl-*a* inversion results of both models were in good agreement with the *in-situ* Chl-*a* concentrations in the study area (Figure 3), with R^2 of 0.9065 and 0.8338, and $RMSE$ of 0.5377 $\mu\text{g/L}$ and 0.6284 $\mu\text{g/L}$, respectively. Although both models can better reflect the overall distribution of Chl-*a* in the Zhoushan archipelago area, the 2 m resolved GF-6/PMS data can observe more detailed changes in Chl-*a*. Therefore, they can be combined together to study the distribution trend of Chl-*a* in the islands area.

Chl-*a* concentration in the nearshore waters of the Zhoushan archipelago is mainly in the range of 1-7 $\mu\text{g/L}$ (Figure 4). Chl-*a* concentration in the west of 122°20'E (region I in Figures 4K, N, O) near the coastal islands is higher with the Chl-*a* value of 3.5-7 $\mu\text{g/L}$, mainly distributes in the Zhoushan archipelago area and the nearshore of Ningbo. Chl-*a*

TABLE 6 Band combination inversion model of Chl-*a*.

Band combination (X)	Function	Fitting model	R^2	RMSE ($\mu\text{g/L}$)
(B2 - B3)/(B2 + B3)	Linear	$y = -27.09 x + 4.675$	0.7760	0.8203
	Power	-	-	-
	Exponential	$y = \exp(-6.219 x + 1.467)$	0.8498	0.1474
	Exponential	-	-	-
B1 * B2/B3	Linear	$y = -63.48 x + 13.42$	0.7076	0.9371
	Power	$y = 0.1011 x^{-1.895}$	0.7180	0.9204
	Exponential	$y = \exp(-14.5 x + 3.465)$	0.7675	0.1833
	Exponential	$y = \exp(0.0963 x^{-1.351})$	0.7598	0.1863
B2/B3 + B1	Linear	$y = -12.17 x^2 + 18.6$	0.7508	0.8652
	Power	$y = 6.887 x^{-3.775}$	0.8352	0.7035
	Exponential	$y = \exp(-2.801 x + 4.671)$	0.8257	0.1587
	Exponential	$y = \exp(1.941 x^{-2.531})$	0.8769	0.1334
B3/(B1 + B2)	Linear	$y = 22.56 x^2 - 8.551$	0.7666	0.8373
	Power	$y = 25.48 x^{3.294}$	0.8023	0.7706
	Exponential	$y = \exp(5.167 x - 1.563)$	0.8358	0.1541
	Exponential	$y = \exp(4.697 x^{2.223})$	0.8509	0.1468
B3/B2	Linear	$y = 14.09 x - 9.527$	0.8003	0.7745
	Power	$y = 4.214 x^{3.677}$	0.8495	0.6723
	Exponential	$y = \exp(3.221 x - 1.78)$	0.8690	0.1376
	Exponential	$y = \exp(1.401 x^{2.423})$	0.8901	0.1260
B3 - B2	Linear	$y = 74.34 x + 4.624$	0.7872	0.7995
	Power	-	-	-
	Exponential	$y = \exp(17.06 x + 1.455)$	0.8612	0.1416
	Exponential	-	-	-

The bold part of the text is the best inversion model based on the power exponential function of the ratio of B2 and B3. "-" means that there is no corresponding functional relationship here.

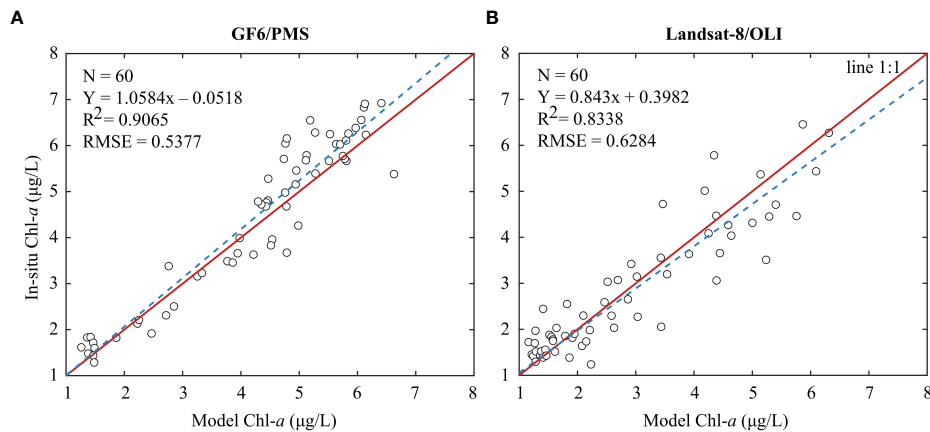


FIGURE 3

Correlation analysis between model and *in-situ* Chl-*a* values. (A) Comparison of Chl-*a* value of GF-6/PMS model with *in-situ* Chl-*a* value; (B) Comparison of Chl-*a* value of Landsat8/OLI model with *in-situ* Chl-*a* value. The x coordinate is the reference value, the y coordinate is the *in-situ* value, and the unit is µg/L.

concentration in the waters within the longitude range of 122° 20'E-122°40'E (region II in Figures 4K, N, O) is lower than in the west and the east area. Chl-*a* concentration in the waters within the longitude range of 122°40'E-123°00'E (region III in Figures 4K, N, O) increased compared to Region II.

Chl-*a* concentration changes with the change of tidal current. When the ocean current passes through islands, regardless of flooding or ebbing, Chl-*a* concentration downstream is generally higher than that upstream (Figure 4).

Chl-*a* concentration in the nearshore waters of the Zhoushan archipelago varies with season. Chl-*a* concentration is higher in spring (April and May) (Figures 4B, G, J, K, N, O) and summer (June and August) (Figures 4C, H, L, P), with the Chl-*a* value in the range of 2-7 µg/L. It is lower in autumn (October and November) (Figures 4D, E, I) and early spring (March) (Figures 4A, M), with the Chl-*a* value in the range of 1-5.5 µg/L; and the lowest Chl-*a* concentration in winter (Figure 4F), with the Chl-*a* value of 2-4 µg/L.

3.3 Details of Chl-*a* variation obtained from GF-6/PMS in islands area

The detailed variation of Chl-*a* in the waters around islands retrieved from the high spatial resolution (2 m) GF-6/PMS images was observed. The four areas of Qushan Islands (Figure 5A), Chuanhu archipelago (Figure 5B), Xizhai and Dongzhai Islands (Figure 5C), and Shengsi archipelago (Figure 5D) were analyzed as examples.

Chl-*a* concentration in the waters around the islands was higher than in the waters farther away (Figure 5), which is in good agreement with previous studies (Zhu et al., 2014; Fu et al.,

2019). The high Chl-*a* concentration area is mainly distributed downstream of the islands (Figures 5A-C). Downstream of the islands, there exists a wake of high Chl-*a* concentration, which is consistent with the direction of the current, and Chl-*a* concentration decreases with increasing distance away from the island. In addition, Chl-*a* concentration along the track of the vortex downstream is also higher than that in the surrounding waters (Figure 6).

There was a significant increase in Chl-*a* concentration upstream and downstream of the island as the current flowing through the island (Figures 6D-F). Chl-*a* increased over distances of 0.12-1.08 km upstream and 2.80-6.84 km downstream, with Chl-*a* concentration increasing over shorter distances upstream than downstream (Figures 6A-C).

3.4 The distribution of fishery resources in Zhoushan archipelago area

Spawning areas of four economic fish species, including Silver pomfret (*Pampus argenteus*, Stromateidae) in April-June (Figure 7A), Japanese anchovy (*Engraulis japonicus*, Enraulidae) in May-June (Figure 7B), Croaker (*Miichthys*, Sciaenidae) in August-October (Figure 7C), and Cuttlefish (*Sepiella maindroni*, Sepiidae) in April-May (Figure 7D) were mainly concentrated in Zhoushan archipelago centered area. Spawning time was mainly in spring and summer, consistent with the appearance of high Chl-*a* in this area. The feeding grounds are relatively broad, mainly in shallow waters within 50 m isobaths (Figure 7).

The density of fish eggs and larvae increased in spring and summer in islands and nearshore waters and decreased significantly in autumn (Figures 8, 9). In the six cruise survey

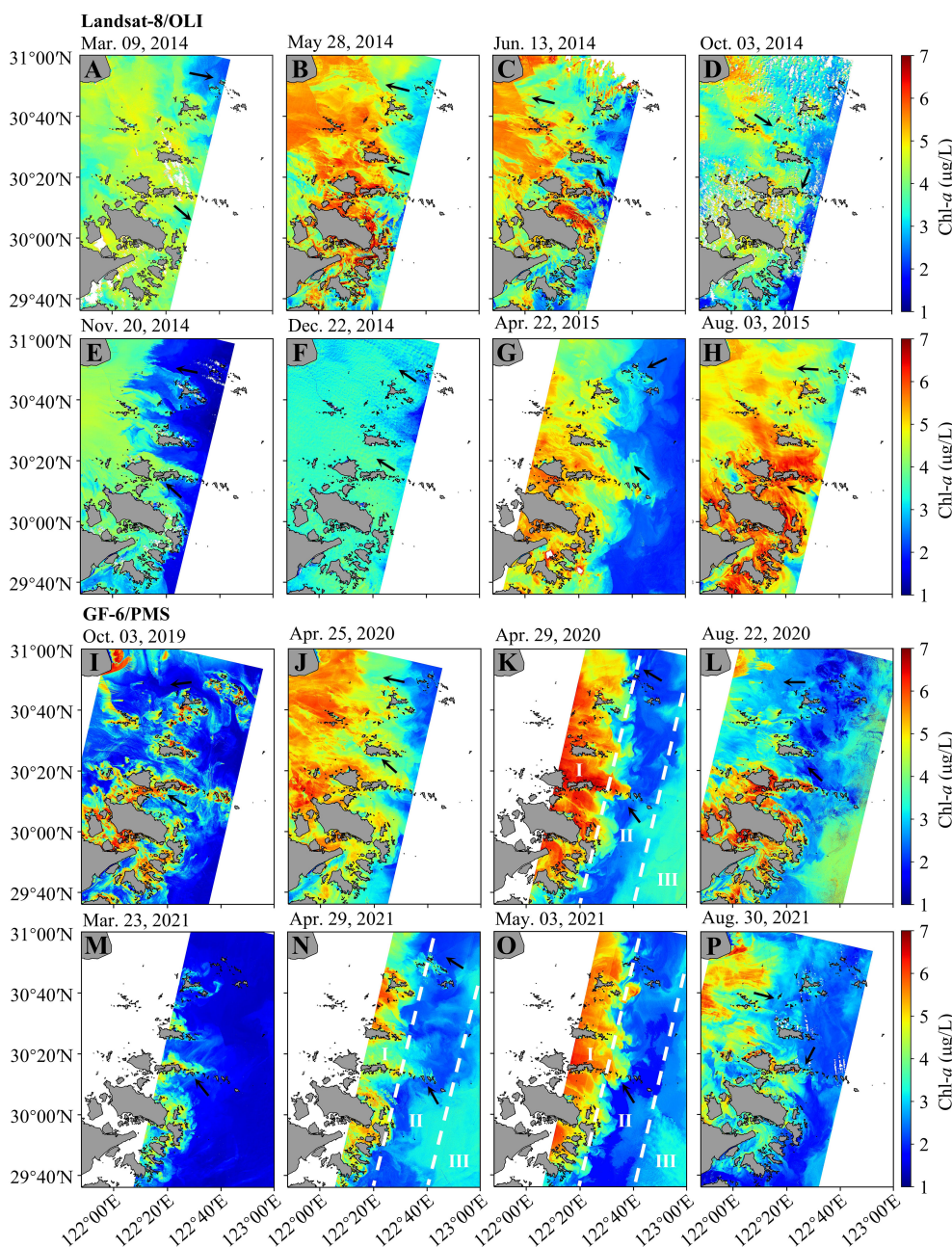


FIGURE 4
 Distribution of Chl-a concentration in Zhoushan archipelago. (A-H) Chl-a obtained from Landsat-8/OLI; (I-P) Chl-a obtained from GF-6/PMS. Black arrow: the direction of the local current. Three regions I (the west of 122°30'E), II (122°30'E-122°50'E), and III (122°50'E-123°E) are delineated in (K, N, O).

collections, the lowest monthly mean density of fish eggs and larvae was reached in November 2014 (Figures 8G, H), with an average density of 0.01 ind./m³ for fish eggs and 0.005 ind./m³ for larvae. The highest monthly mean density value occurred in June 2014 (Figures 8E, F), with an average density of 0.27 ind./m³ for fish eggs and 0.21 ind./m³ for larvae.

Chl-a concentration in the study area also showed seasonal variations during the same period (Figure 9), with high values of Chl-a in spring (April, May) and summer (June, August), with an average monthly Chl-a concentration ranging from 4.31-4.80 µg/L. In contrast, there was a relatively low Chl-a concentration in early spring (March) and autumn (November), with an

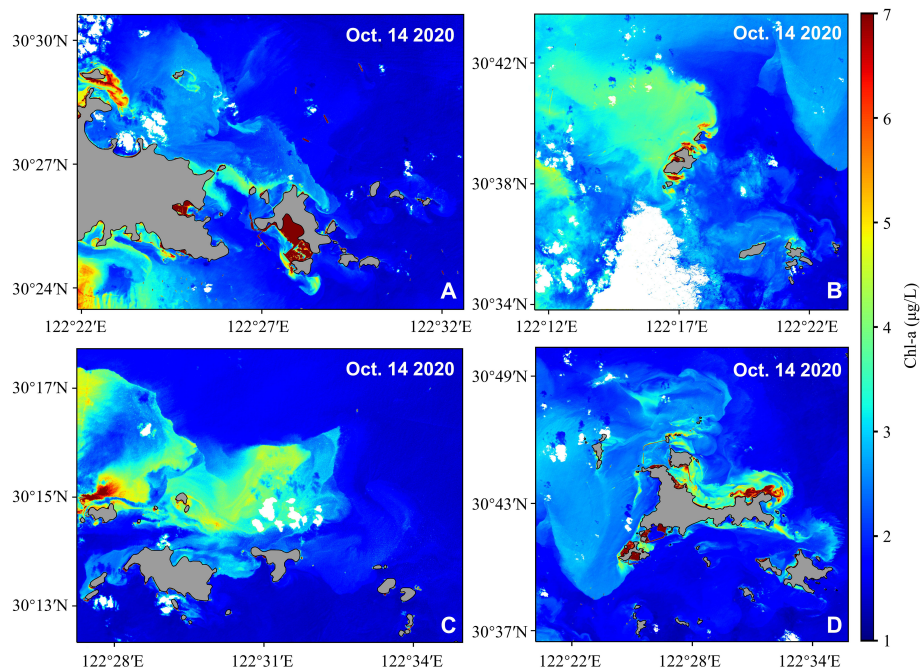


FIGURE 5

Chl-*a* concentration distribution details around the water of Zhoushan archipelago. Chl-*a* distribution in the figure is taken from the GF-6/PMS image on 14 October 2020 and the Chl-*a* concentration retrieved based on the new model of PMS-Chl-*a*. (A) The Qushan Islands; (B) the Chuanhu archipelago; (C) the Xizhai and Dongzhai Islands; (D) the Shengsi archipelago.

average monthly Chl-*a* concentration ranging from 2.84–3.52 µg/L.

High and low changes in the biomass density of fish eggs and larvae in the water of the Zhoushan archipelago show a high degree of consistency with the spatial distribution and seasonal variation of Chl-*a* concentration in the study area waters.

4 Discussion

4.1 The applicability of the new Chl-*a* model

The water in the Zhoushan archipelago area is class II water. The spectral properties of Chl-*a* are affected by colored dissolved organic matter (CDOM), SSC, and the traditional blue-green band ratio (or combination) algorithm will no longer be suitable for the inversion of Chl-*a* in class II water (Sathyendranath et al., 1989; Bowers et al., 1996). It was found that the NIR band showed a high correlation with SSC in highly turbid waters, and the magnitude of the correlation increased with the concentration of suspended matter (Tao et al., 2007; Zhu et al., 2020). Therefore, B4 (NIR) was excluded in building the Chl-*a* inverse model.

Empirical algorithms are still valid for remote sensing ocean color in complex estuaries and nearshore waters (Zhu et al., 2015). The impact of SSC on the Chl-*a* inversion was effectively reduced by introducing a power exponential form of the red and red-green bands ratio ($(B3/B2)^a$), which is consistent with previous studies (Ma et al., 2005; Tzortziou et al., 2007; Le et al., 2013) as well as our study.

The best band combination was selected to build the Chl-*a* model, and the Chl-*a* inversion results of the PMS-Chl-*a* model were in good agreement with the *in-situ* Chl-*a* concentration in the study area (Figure 3A). Furthermore, the modeled Chl-*a* in other seasons using the newly built model was consistent with the Chl-*a* distribution in the corresponding season in prior studies (Ji et al., 2018; Fu et al., 2019). Therefore, the new Chl-*a* model is applicable in the study area in all seasons.

It was found that detailed variation in Chl-*a* vortex belts downstream of the islands was revealed in the GF-6/PMS (2 m) particular resolution image (Figure 10A), which was not clearly shown in the Landsat-8/OLI (30 m) medium resolution satellite data (Figure 10B). Therefore, GF-6/PMS (2 m) high spatial resolution satellite data play a crucial role in studying the distribution of Chl-*a* details in the waters around islands.

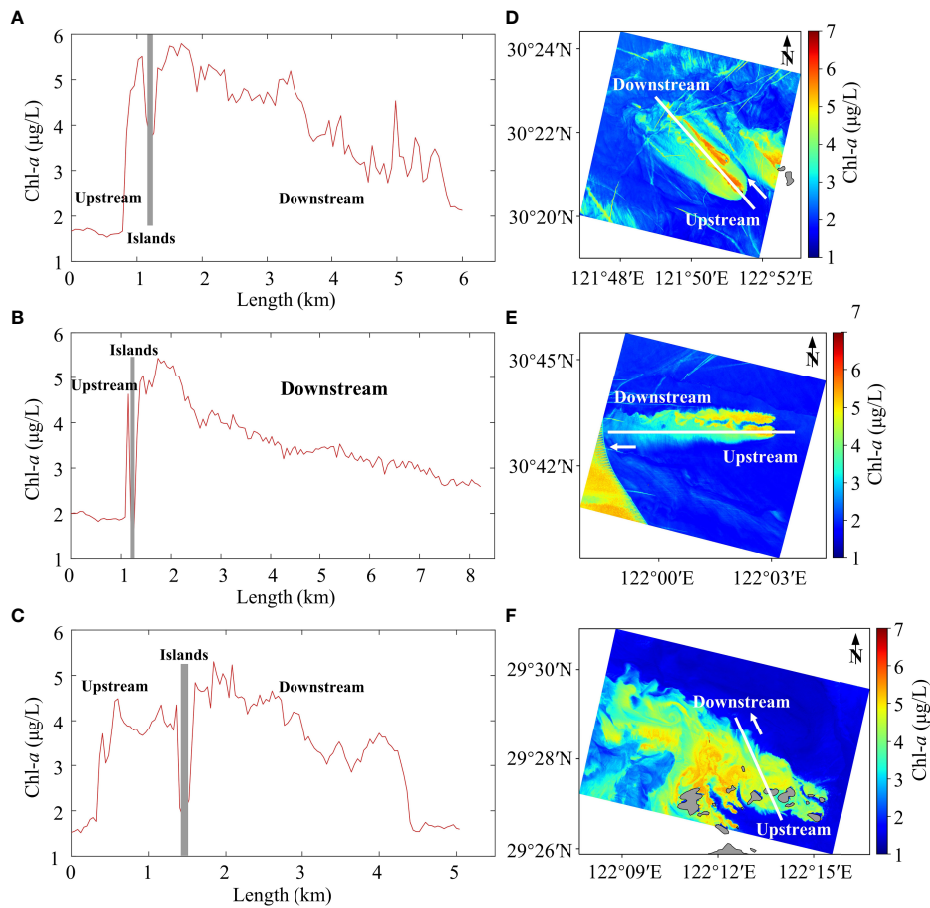


FIGURE 6

The variation in Chl-*a* concentrations upstream and downstream of the islands. (A–C) Chl-*a* concentration variation trends upstream and downstream of the islands on the white line transect; (D–F) Chl-*a* concentration distribution in waters adjacent to islands. Grey vertical bars: islands.

4.2 Seasonal factors contribute to Chl-*a* and fishery resources

The seasonal variation of environmental factors such as SST, wind, and SSS in the study area (Chen and Liu, 2015) also contribute to Chl-*a* and fishery resources.

In spring, the Taiwan warm current gradually increases in strength northward (Figure 11I), delivering phosphate-rich hypersaline water to the nearshore waters of Zhoushan archipelago. In addition, SST in the study area rebounded in spring (March–May) and summer (June–August), providing more suitable conditions for the growth and reproduction of phytoplankton. Zhoushan has a predominantly north subtropical monsoon climate with south winds prevailing in spring and summer under the influence of the East Asian monsoon (Figure 11E, F) (Fu et al., 2019). This wind direction was favorable for forming coastal zone upwelling (Ding, 1985; Hu and Zhao, 2007). In the wind-induced upwelling area in the nearshore waters of the Zhoushan archipelago (Figures 11A, B),

the upwelling brings the nutrient-rich middle and lower waters of the study area to the strong photosynthetic layer, providing sufficient nutrients and favorable growth conditions for phytoplankton and zooplankton, which in turn attracts a large number of fish aggregations to breed here (Oliveira et al., 2009; Fernando et al., 2018). Islands induced the change of water environmental factors also contribute to fishery development. In addition, the summer coincides with the peak runoff of the Yangtze River, whose diluted water continuously expands eastward under the action of its substantial runoff and southwest monsoon (Figure 11J). Flushing water carried abundant nutrients, which facilitated phytoplankton growth and fish reproduction (Wang et al., 2008; Xu et al., 2020). The light conditions also significantly affect Chl-*a* concentration (Oliver et al., 2010; Garbulsky et al., 2014).

The salinity of the study sea decreased (Figure 11K, L) in autumn (September–November) and winter (December–February) when the low saline water tongue of the Yangtze estuary extended to the southwest under the influence of

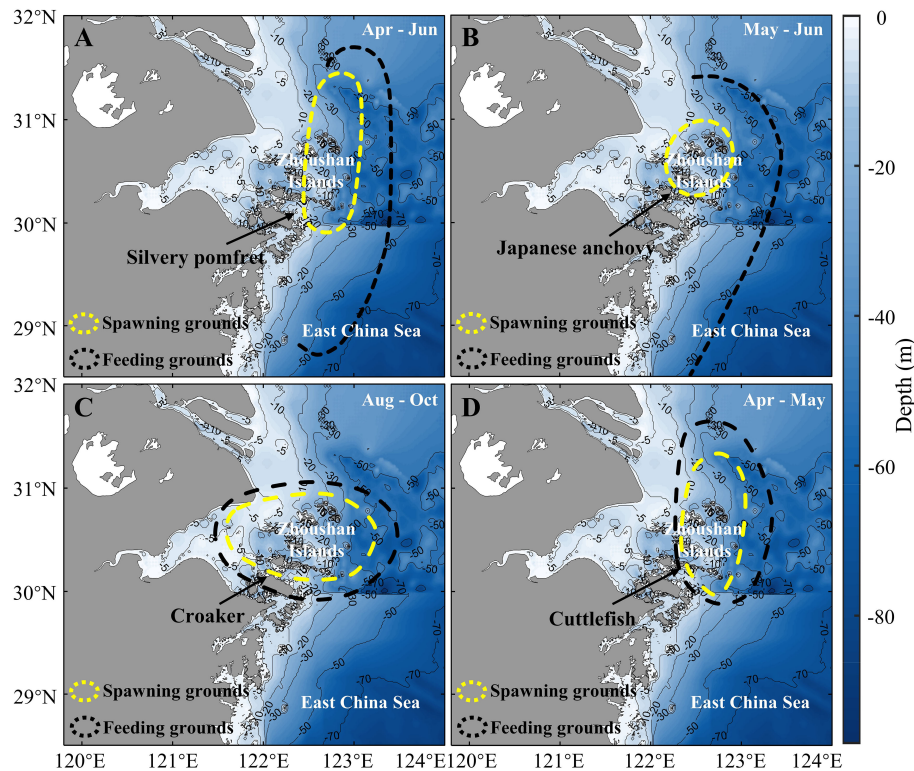


FIGURE 7 Spawning grounds and feeding grounds for various fish species in the Zhoushan Archipelago Sea area. (A) Silver pomfret; (B) Japanese anchovy; (C) Croaker; (D) Cuttlefish. Yellow circles: spawning grounds; black circles: feeding grounds.

northeasterly winds (Figure 11G, H). Although the southward moving flushing water brought nutrients to the study sea, the disappearance of the upwelling (Figure 11C, D) caused a weakening of convective mixing and a significant decrease in biomass (Hu and Zhao, 2007; Oliveira et al., 2009). Moreover, the reduced light in the East China Sea in autumn and winter limits the growth of phytoplankton (Oliver et al., 2010; Garbulska et al., 2014), resulting in lower Chl-*a* concentration in autumn and winter than in spring and summer.

The significant differences in the seasonal distribution of Chl-*a* and fishery resources show certain consistency of variation with the monsoon, the nutrient supplies, the temperature, light conditions, and so on.

4.3 Other factors contribute to Chl-*a* and fishery resources

The nearshore waters of the Zhoushan area are one of the strong coastal tidal areas in China, and the change of Chl-*a* in the study area is closely related to the specific hydrodynamic conditions (currents) of the water (Wolanski and Hamner, 1988; Lévy et al., 2012; Everett et al., 2014).

The current in the study area is characterized by stable irregular semi-daily tides (Figure 12), with two flood and ebb tides in a day. Current speed and direction vary regularly with time (Chen et al., 1990). Similar patterns and tidal features are repeated daily (Cao and Lin, 2000). The tide of any day can be taken as an example to illustrate the changing rules of flooding and ebbing tide in the study area. Due to data limitations, the sea surface current data for the Zhoushan archipelago are taken from November 2020. The study area is dotted with intensive islands, and the coastline is intricate and narrow. The currents are blocked and rubbed by the islands and the seabed, causing strong turbulence around the islands, resulting in some degree of upwelling upstream of the islands and eddies downstream (Wolanski and Hamner, 1988). The isobaths of the nearshore waters of the Zhoushan archipelago are densely distributed, basically parallel to the shoreline and islands, and the topography of the seabed is mostly flat and open (Figure 7) with a depth of 10–50 m, which is an excellent place for marine fishery production (Chang et al., 2012). Its strong semidiurnal tide interacts with the islands, causing regular changes in Chl-*a* (Liu et al., 2012).

Upstream of the islands, the formation of upwelling prompts the vertical exchange of waters near the islands. Nutrients and

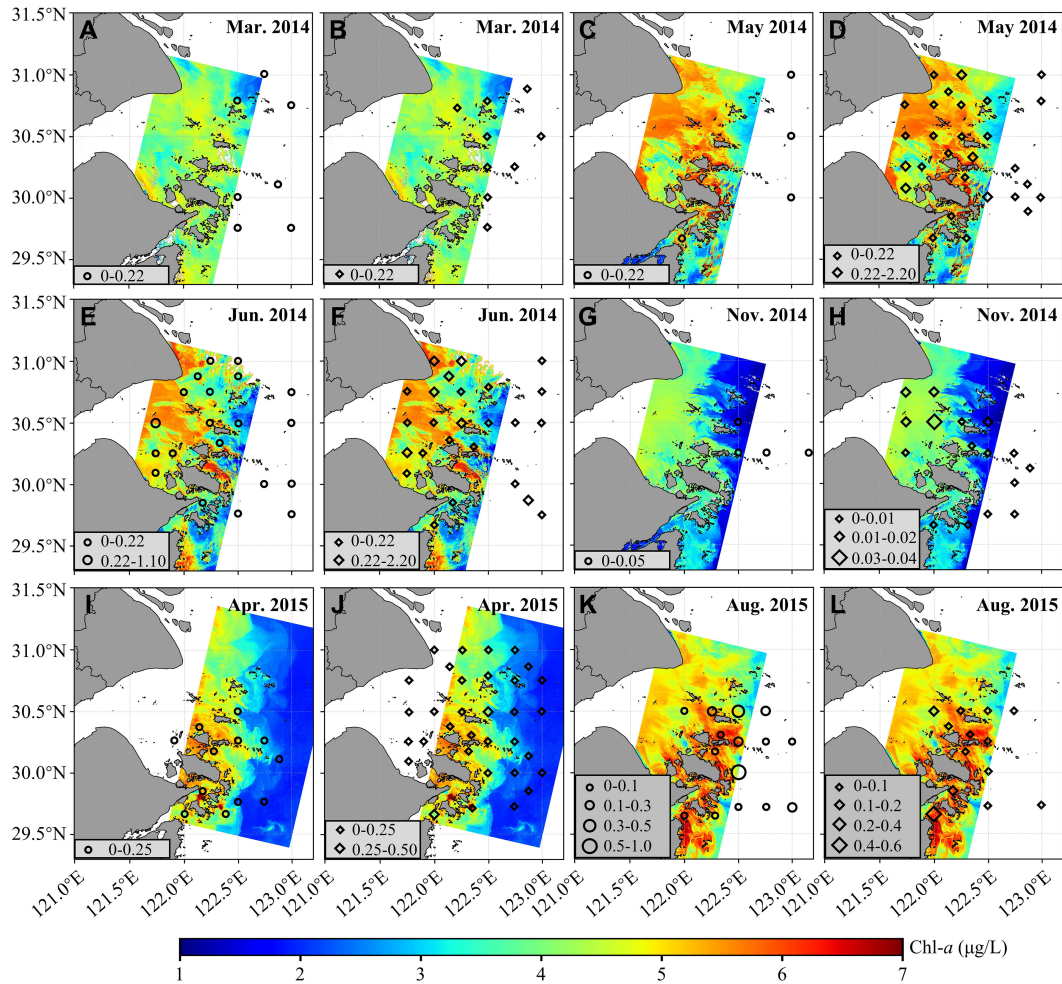


FIGURE 8
The density (ind./m³) of fish eggs and larvae in spring, summer and autumn in the water of the Zhoushan archipelago from 2014 to 2015. (A–D) In spring; (E, F) in summer; (G, H) in autumn; (I, J) in spring; (K, L) in summer. Black round dots: larvae; black diamond-shaped dots: fish eggs.

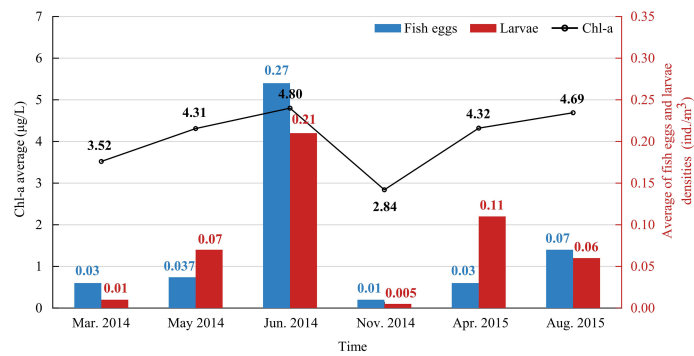


FIGURE 9
Temporal correlation between the biomass density of fish eggs and larvae and Chl-a concentration in the water of the Zhoushan archipelago.

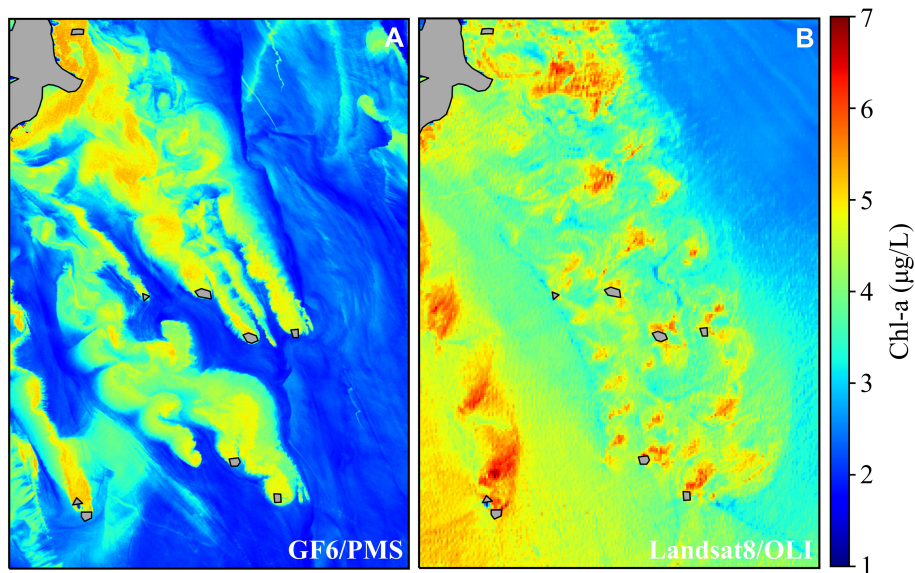


FIGURE 10

Comparison of the detailed distribution of Chl-*a* concentrations in the waters around islands on GF-6/PMS and Landsat8/OLI images. (A) Distribution of Chl-*a* concentration in GF-6/PMS image; (B) distribution of Chl-*a* concentration in landsat-8/OLI image.

other substances on the seabed are turned up and spread, causing the low-temperature, high-salinity, nutrient-rich seawater from the bottom and near-bottom layers to rise continuously to the surface. This accelerates the rate of nutrient circulation and causes an increase in plankton and improved water quality, allowing fish to congregate here (Simon, 1989; Howe, 2003). The downstream of the islands generate Karman vortex streets eddies, the vertical velocity generated by the eddies carries deep nutrients to the photic zone, allowing phytoplankton to grow, attracting fish (Wolanski and Hamner, 1988; Thomson et al., 2009; Everett et al., 2014).

Studies have shown that fish movement and habitat are correlated with changes in currents in island areas and that island disturbance of currents and their biological effects on coastal ecosystems are important (Harlan et al., 2002; Caldeira and Sangra, 2012).

Based on the analysis above, intensive islands create not only an ideal environment for nutrients, which is conducive to the proliferation of phytoplankton here, making the overall Chl-*a* concentration values in the waters around the islands higher than in the waters further offshore. It also creates different water flow conditions for fish, providing excellent shelter, baiting grounds, breeding grounds, or habitats for fish, thus impacting the increase of fishery resources.

Therefore, all the environmental factors combine, contributing to fish eggs and larvae density. Chl-*a* change details can be well revealed by high-resolution satellite data and show consistency with the spatial distribution and seasonal variation of fish eggs and larvae in the water of the Zhoushan

archipelago. This indicates that the distribution of Chl-*a* can help us analyze and find the spawning grounds.

5 Conclusion

This study established a new Chl-*a* inversion model based on *in-situ* data and GF-6/PMS satellite data using the ratio relationship between B2(green) and B3(red). Chl-*a* distribution details in the water of the Zhoushan archipelago were analyzed. High Chl-*a* concentration is mainly concentrated in the nearshore islands area. Chl-*a* concentration changes obviously with the change of tidal currents, with higher Chl-*a* concentration appearing around islands, especially downstream of islands. There appears a significant increase in Chl-*a* concentration both upstream and downstream of the islands as the current flows through the islands. Temporally, Chl-*a* concentration is higher in spring and summer, lower in autumn, and the lowest Chl-*a* concentration in winter.

The fish species that spawn in the waters of the Zhoushan archipelago are abundant, and the change of fish eggs and larvae in the waters shows consistency with the spatial distribution and seasonal variation of Chl-*a* (Figure 13).

Island interacts with current resulting in the diverse currents (upstream upwelling and tidal current downstream vortex currents) around the islands, promoting the vertical exchange of water and the uplifting of nutrients, resulting in the increase of Chl-*a* concentration in the waters around the islands. The

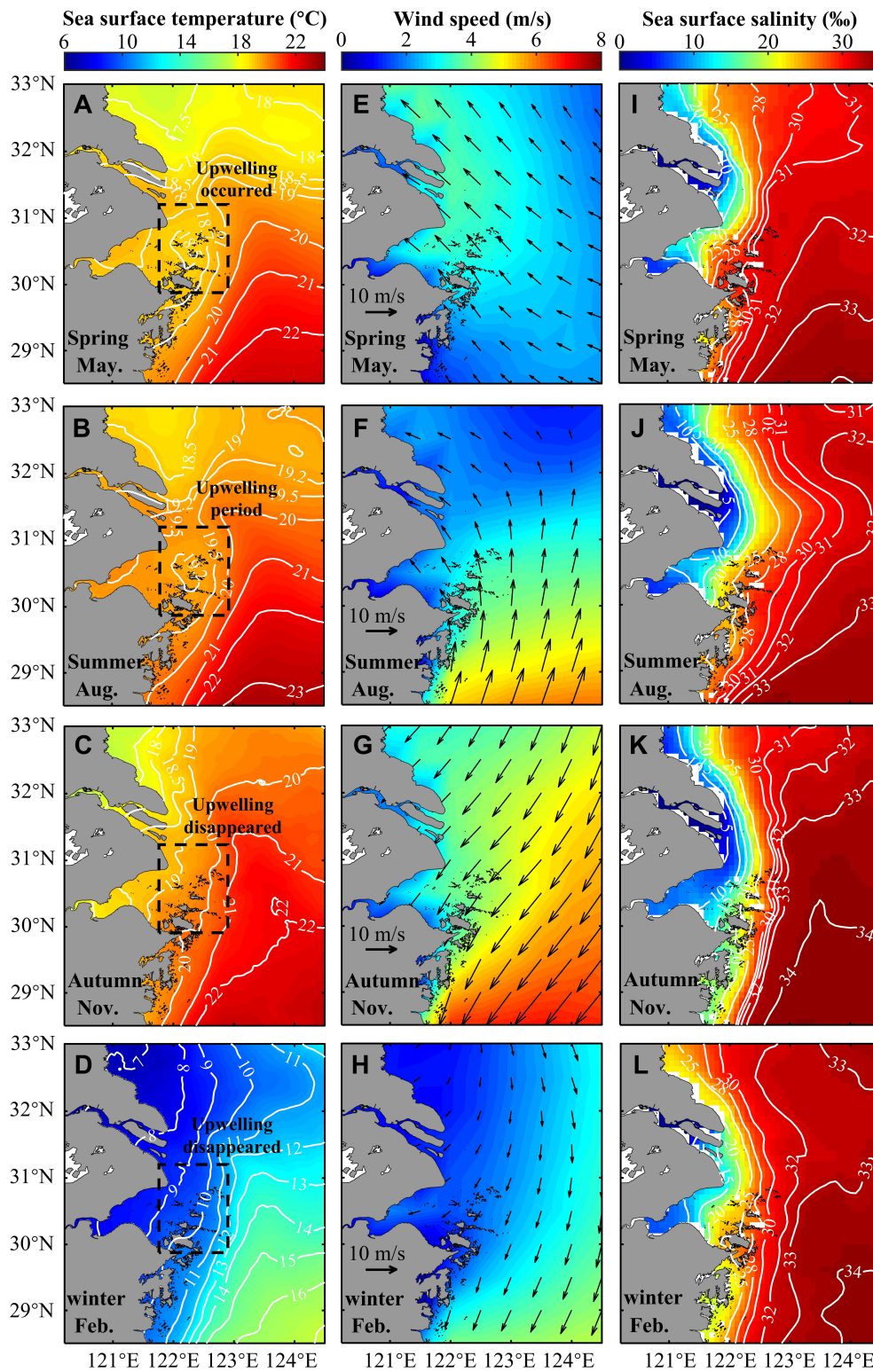


FIGURE 11
The seasonal variation of SST, wind and SSS for Zhoushan archipelago in 2020. (A–D) SST; (E–H) 10 m wind at the sea surface; (I–L) SSS. The black square is the study area.

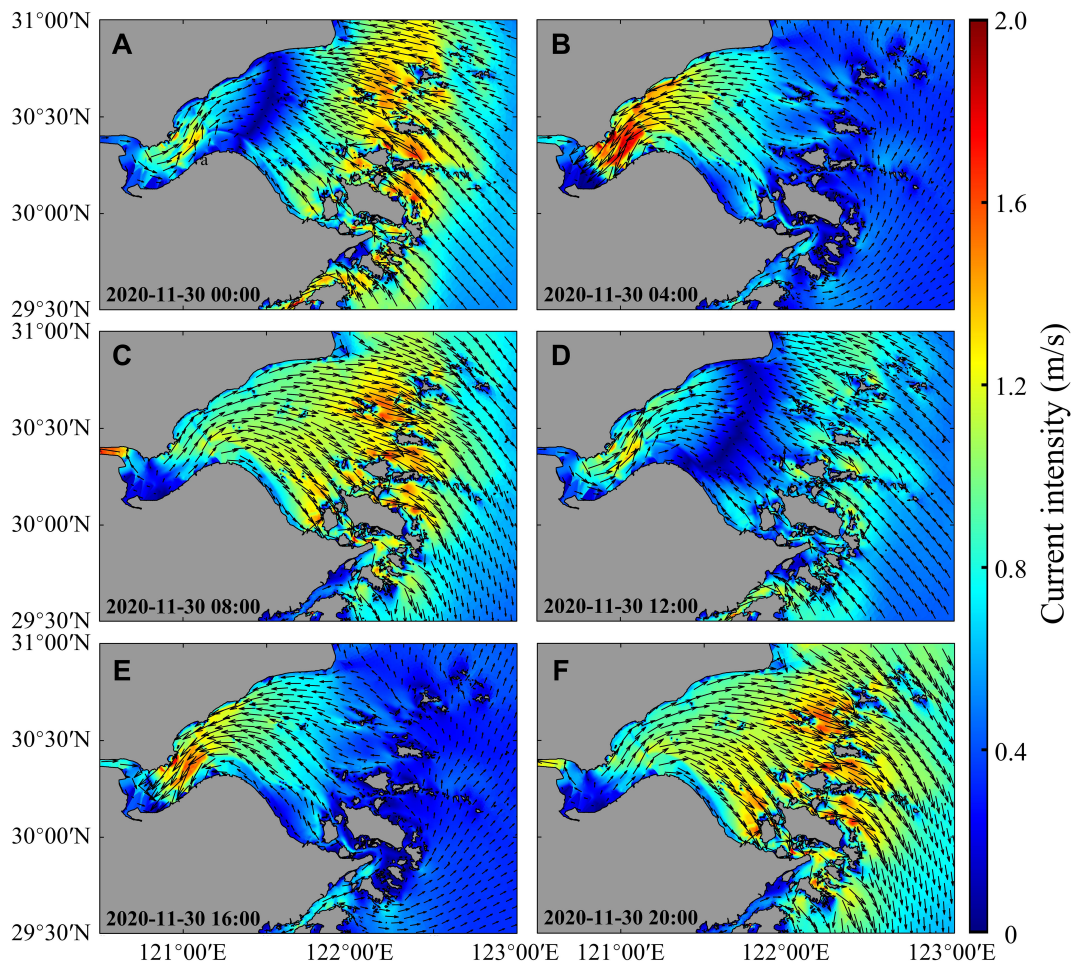


FIGURE 12 Distribution of currents on the sea surface of Zhoushan archipelago on November 30, 2020. (A) 00:00; (B) 10 m wind at the sea surface; (C) SSS. (A–F) Distribution of currents at 00:00, 04:00, 08:00, 12:00, 16:00, and 20:00, divided by four-hourly intervals.

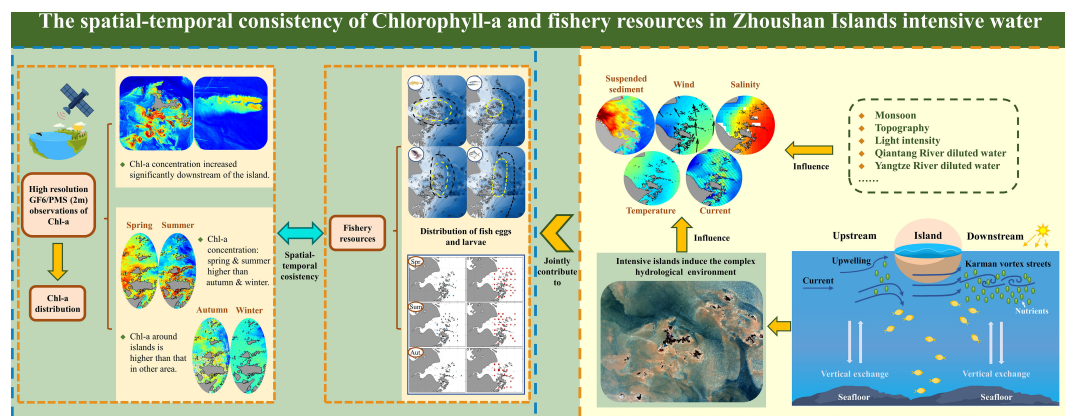


FIGURE 13 The spatial-temporal consistency of Chlorophyll-a and fishery resources in Zhoushan Islands intensive water.

diverse flow conditions, the ideal nutrient-rich environment, and the abundant phytoplankton attract a large number of fishes to gather and breed in the waters around the islands. In addition, many seasonal factors also affected the Chl-*a* concentration distribution and fish eggs and larvae biomass density. Its unique hydrological environment, topography, and hydrodynamic conditions are the basis for forming the Zhoushan fishing ground.

Data availability statement

The original contributions presented in the study are included in the article/supplementary material. Further inquiries can be directed to the corresponding author.

Author contributions

LC conducted the research design, data collecting, analysis, and manuscript writing. RT conducted the data processing, and manuscript writing. XY conducted the data collecting and research advisement. YZ the data collecting, analysis. JJ assisted data collecting. MY assisted data collecting. All authors have read and agreed to the published version of the manuscript.

Funding

This work was supported by the Zhejiang Key Science and Technology Project (2020C02004); the National Natural Science Foundation of China Key international (regional)

References

- Bacher, C., Grant, J., Hawkins, A. J. S., Fang, J. G., Zhu, M. Y., and Besnard, M. (2003). Modelling the effect of food depletion on scallop growth in sunago bay (China). *Aquat. Living Resour.* 16, 10–24. doi: 10.1016/S0990-7440(03)00003-2
- Barbieri, M. A., Silva, C., Larouche, P., Nieto, K., and Yáñez, E. (2004). Detection of mesoscale oceanic features using radarsat-1 AVHRR and SeaWiFS images and the possible link with jack mackerel (*Trachurus murphyi*) distribution in central Chile. *Gayana* 68, 29–39. doi: 10.4067/S0717-65382004000200006
- Bierman, P., Lewis, M., Ostendor, B., and Tanner, J. (2011). A review of methods for analysing spatial and temporal patterns in coastal water quality. *Ecol. Indic.* 11, 103–114. doi: 10.1016/j.ecolind.2009.11.001
- Bowers, D. G., Harker, G. E. L., and Stephan, B. (1996). Absorption spectra of inorganic particles in the Irish Sea and their relevance to remote sensing of chlorophyll. *Int. J. Remote Sens.* 17, 2449–2460. doi: 10.1080/01431169608948782
- Cai, L. N., Bu, J., Tang, D. L., Zhou, M. R., Yao, R., and Huang, S. Y. (2020). Geosynchronous satellite GF-4 observations of chlorophyll-*a* distribution details in the bohai Sea, China. *Sensors* 20, 5471. doi: 10.3390/s20195471
- Cai, L. N., Zhou, M. R., Liu, J. Q., Tang, D. L., and Zuo, J. (2020). HY-1C observations of the impacts of islands on suspended sediment distribution in zhoushan coastal waters, China. *Remote Sens.* 12, 1766. doi: 10.3390/rs12111766
- Caldeira, R. M. A., and Sangra, P. (2012). Complex geophysical wake flows Madeira archipelago case study. *Ocean Dyn.* 62, 683–700. doi: 10.1007/s10236-012-0528-6
- Cao, Y., and Lin, B. Y. (2000). Tidal characteristics of hangzhou bay. *Zhejiang Wat. Cons Hydr. Coll. (in Chinese)* 12, 14–16.
- Chang, N. N., Shiao, J. C., and Gong, G. C. (2012). Diversity of demersal fish in the East China Sea: implication of eutrophication and fishery. *Cont. Shelf Res.* 47, 42–54. doi: 10.1016/j.csr.2012.06.011
- Chen, C., Beardsley, R. C., and Cowles, G. (2006). An unstructured grid, finite-volume coastal ocean model (FVCOM) system. *Oceanography* 19, 78–89. doi: 10.5670/oceanog.2006.92
- Chen, J., and Liu, J. L. (2015). The spatial and temporal changes of chlorophyll-*a* and suspended matter in the eastern coastal zones of China during 1997–2013. *Cont. Shelf Res.* 95, 89–98. doi: 10.1016/j.csr.2015.01.004
- Chen, J. Y., Liu, C. Z., Zhang, C. L., and Herndon, J. W. (1990). Geomorphological development and sedimentation in qiantang estuary and hangzhou bay. *J. Coast. Res.* 6, 559–572. doi: 10.2307/4297719
- Chen, J., Zhang, X. H., and Quan, W. T. (2013). Retrieval chlorophyll-*a* concentration from coastal waters: three-band semi-analytical algorithms

cooperative research project (42020104009); the National Key Research and Development Program (2019YFD0901205); the Basic Public Welfare Research Program of Zhejiang Province (LGF21D010004); the Research on group ideological and political subject teaching model of ocean remote sensing (132); the Science Foundation of Donghai Laboratory (DH-2022KF01010).

Acknowledgments

The authors would like to thank NSOAS for providing the data free of charge. The authors wish to thank the national satellite ocean application center, China and Sophisticated Ocean Front and Fisheries Investigation (SOPHI) for the data support.

Conflict of interest

The authors declare that the research was conducted in the absence of any commercial or financial relationships that could be construed as a potential conflict of interest.

Publisher's note

All claims expressed in this article are solely those of the authors and do not necessarily represent those of their affiliated organizations, or those of the publisher, the editors and the reviewers. Any product that may be evaluated in this article, or claim that may be made by its manufacturer, is not guaranteed or endorsed by the publisher.

- comparison and development. *Opt. Express*. 21, 9024–9042. doi: 10.1364/oe.21.009024
- Dall'Olmo, G., Gitelson, A. A., Rundquist, D. C., Leavitt, B., Barrow, T., and Holz, J. C. (2005). Assessing the potential of SeaWiFS and MODIS for estimating chlorophyll concentration in turbid productive waters using red and near-infrared bands. *Remote Sens. Environ.* 96, 176–187. doi: 10.1016/j.rse.2005.02.007
- Deng, Z. D., Lu, Z., Wang, G. Y., Wang, D. Q., Ding, Z. B., Zhao, H. F., et al. (2021). Extraction of fractional vegetation cover in arid desert area based on Chinese GF-6 satellite. *Open Geosci.* 13, 416–430. doi: 10.1515/geo-2020-0241
- Ding, Z. X. (1985). Influences of wind on vertical structures of temperature and salinity, and upwelling off zhejiang coast in summer. *Chin. J. Oceanol. Limnol.* 3, 109–117. doi: 10.1007/bf02852908
- Duan, H. T., Zhang, Y. Z., Zhang, B., Song, K. S., and Wang, Z. M. (2007). Assessment of chlorophyll-a concentration and trophic state for lake chagan using landsat TM and field spectral data. *Environ. Monit. Assess.* 129, 295–308. doi: 10.1007/s10661-006-9362-y
- Everett, J. D., Baird, M. E., Roughan, M., Suthers, I. M., and Doblin, M. A. (2014). Relative impact of seasonal and oceanographic drivers on surface chlorophyll a along a western boundary current. *Prog. Oceanogr.* 120, 340–351. doi: 10.1016/j.pocean.2013.10.016
- Fernando, D., Tang, D. L., and Xu, H. B. (2018). The propensity of chlorophyll a, sea surface temperature and wind speed in the bay of Bengal. *J. nanjing Univ. Inf. Sci. Technol.* 10, 334–341. doi: 10.13878/j.cnki.jnuist.2018.03.009
- Fu, J. Q., Chen, C., and Chu, Y. L. (2019). Spatial-temporal variations of oceanographic parameters in the zhoushan sea area of the East China Sea based on remote sensing datasets. *Reg. Stud. Mar. Sci.* 28, 100626. doi: 10.1016/j.rmsa.2019.100626
- Fu, Y., Xu, S., Zhang, C., and Sun, Y. (2018). Spatial downscaling of MODIS chlorophyll-a using landsat 8 images for complex coastal water monitoring. *Estuar. Coast. Shelf Sci.* 209, 149–159. doi: 10.1016/j.ecss.2018.05.031
- Garbulska, M. F., Filella, I., Verger, A., and Peñuelas, J. (2014). Photosynthetic light use efficiency from satellite sensors: From global to Mediterranean vegetation. *Environ. Exp. Bot.* 103, 3–11. doi: 10.1016/j.envexpbot.2013.10.009
- Gianinetta, M., and Scaioni, M. (2008). Automated geometric correction of high-resolution pushbroom satellite data. *Photogramm Eng. Remote Sens.* 74, 107–116. doi: 10.14358/PERS.74.1.107
- Habibullah, R., Mubarak, G., and Galib, M. (2020). Analysis of yellowfin tuna (*Thunnus albacares*) fishing ground based on sea surface temperature and chlorophyll-a in the West Sumatra waters. *Asian J. Aquat. Sci.* 3, 236–247. doi: 10.31258/ajoaas.3.3.236-247
- Harlan, J. A., Swearer, S. E., Leben, R. R., and Fox, C. A. (2002). Surface circulation in a Caribbean island wake. *Cont. Shelf Res.* 22, 417–434. doi: 10.1016/S0278-4343(01)00073-5
- Howe, J. C. (2003). Artificial reef evaluation: with application to natural marine habitats. *Fish. Res.* 63, 297–298.
- Huang, L. G., Fang, Y., Zhang, D. W., and Lin, L. S. (2016). Quantitative retrieval of chlorophyll a concentration based on landsat-8 OLI in the lakes. *Jiangxi Sci. (in Chinese)* 34 441–444, 456. doi: 10.13990/j.issn1001-3679.2016.04.009
- Huot, Y., Babin, M., Bruyant, F., Grob, C., Twardowski, M. S., and Claustre, H. (2007). Does chlorophyll a provide the best index of phytoplankton biomass for primary productivity studies? *Biogeosci. Discuss.* 4, 707–745. doi: 10.5194/bgd-4-707-2007
- Hu, M. N., and Zhao, C. F. (2007). Long-time observation of upwelling in the zhoushan islands and adjacent seas during the summer season. *J. Ocean Univ. China.* 37, 235–240. doi: 10.16441/j.cnki.hdx.2007.s1.043
- Jawak, S. D., and Luis, A. J. (2015). A rapid extraction of water body features from Antarctic coastal oasis using very high-resolution satellite remote sensing data. *Aquat. Procedia.* 4, 125–132. doi: 10.1016/j.aqpro.2015.02.018
- Jeffrey, S. W., and Humphrey, G. F. (1975). New spectrophotometric equations for determining chlorophylls a, b, c1 and c2 in higher plants, algae and natural phytoplankton. *Biochem. Physiol. Pflanz.* 167, 191–194. doi: 10.1016/S0015-3796(17)30778-3
- Ji, C. X., Zhang, Y. Z., Cheng, Q. M., Tsou, J. Y., Jiang, T. C., and Liang, X. S. (2018). Evaluating the impact of sea surface temperature (SST) on spatial distribution of chlorophyll-a concentration in the East China Sea. *Int. J. Appl. Earth Obs. Geoinf.* 68, 252–261. doi: 10.1016/j.jag.2018.01.020
- Kim, H. H., Ko, B. C., and Nam, J. Y. (2016). Predicting chlorophyll-a using landsat 8 OLI sensor data and the non-linear RANSAC method – a case study of nakkong river, south Korea. *Int. J. Remote Sens.* 37, 3255–3271. doi: 10.1080/01431161.2016.1196839
- Kourti, N., Shepherd, I., Schwartz, G., and Pavlakis, P. (2001). Integrating spaceborne SAR imagery into operational systems for fisheries monitoring. *Can. J. Remote Sens.* 27, 291–305. doi: 10.1080/07038992.2001.10854872
- Lee, Y. J., Matrai, P. A., Friedrichs, M. A. M., Saba, V. S., Antoine, D., Ardyna, M., et al. (2015). An assessment of phytoplankton primary productivity in the Arctic ocean from satellite ocean color/*in situ* chlorophyll-a based models. *J. Geophys. Res.-Oceans.* 120, 6508–6541. doi: 10.1002/2015JC011018
- Le, C., Hu, C., English, D., Cannizzaro, J., Chen, Z., Feng, L., et al. (2013). Towards a long-term chlorophyll-a data record in a turbid estuary using MODIS observations. *Prog. Oceanogr.* 109, 90–103. doi: 10.1016/j.pocean.2012.10.002
- Le, C. F., Li, Y. M., Zha, Y., Sun, D. Y., Huang, C. C., and Lu, H. (2009). A four-band semi-analytical model for estimating chlorophyll a in highly turbid lakes: the case of taihu lake, China. *Remote Sens. Environ.* 113, 1175–1182. doi: 10.1016/j.rse.2009.02.005
- Lévy, M., Ferrari, R., Franks, P. J. S., Martin, A. P., and Rivière, P. (2012). Bringing physics to life at the submesoscale. *Geophys. Res. Lett.* 39, 1–13. doi: 10.1029/2012GL052756
- Liang, J., Wang, W. D., Xu, H. X., Zhou, Y. D., Xu, K. D., Zhang, H. L., et al. (2020). Diel and seasonal variation in fish communities in the zhongshieshan marine island reef reserve. *Fish. Res.* 227, 105549. doi: 10.1016/j.fishres.2020.105549
- Lin, Y., Ye, Z. L., Zhang, Y., and Yu, J. (2016). Spectral feature analysis for quantitative estimation of cyanobacteria chlorophyll-a. *Int. Arch. Photogramm Remote Sens. Spat. Inf. Sci. XLI-B7*, 12–19. doi: 10.5194/isprs-archives-XLI-B7-91-2016
- Liu, S. F., Liu, Y. G., Yang, G., Qiao, S. Q., Li, C. X., Zhu, Z. W., et al. (2012). Distribution of major and trace elements in surface sediments of hangzhou bay in China. *Acta Oceanol. Sin.* 31, 89–100. doi: 10.1007/s13131-012-0223-y
- Ma, C. F., Jiang, X. W., Tang, J. W., Wang, X. M., Li, T. J., Huang, H. J., et al. (2005). Inverse algorithms of ocean constituents for HY-1/CCD broadband data. *Haiyang xuebao. (in Chinese)*, 38–44.
- Moses, W. J., Gitelson, A. A., Berdnikov, S., and Povazhnyy, V. (2009). Satellite estimation of chlorophyll-a concentration using the red and NIR bands of MERIS—the Azov Sea case study. *IEEE Geosci. Remote Sens. Lett.* 6, 845–849. doi: 10.1109/lgrs.2009.2026657
- Nazeer, M., and Nichol, J. E. (2016). Development and application of a remote sensing-based chlorophyll-a concentration prediction model for complex coastal waters of Hong Kong. *J. Hydrol.* 532, 80–89. doi: 10.1016/j.jhydrol.2015.11.037
- Oliveira, P. B., Nolasco, R., Dubert, J., Moita, T., and Peliz, A. (2009). Surface temperature, chlorophyll and advection patterns during a summer upwelling event off central Portugal. *Cont. Shelf Res.* 29, 759–774. doi: 10.1016/j.csr.2008.08.004
- Oliver, R. L., Mitrovic, S. M., and Rees, C. (2010). Influence of salinity on light conditions and phytoplankton growth in a turbid river. *River Res. Appl.* 26, 894–903. doi: 10.1002/rra.1309
- Pan, X., Yang, Z., Yng, Y. B., and Sun, Y. X. (2022). Comparison and applicability analysis of methods for extracting cyanobacteria from Lake Taihu based on GF-6 data. *J. Lake Sci.* 34, 1–12. doi: 10.18307/2022.060
- Paulino, C., Segura, M., and Chacón, G. (2016). Spatial variability of jumbo flying squid (*Dosidicus gigas*) fishery related to remotely sensed SST and chlorophyll-a concentration 2004–2012. *Fish. Res.* 173, 122–127. doi: 10.1016/j.fishres.2015.10.006
- Perkins, T., Adler-Golden, S., Matthew, M., Berk, A., Anderson, G., Gardner, J., et al. (2005). “Retrieval of atmospheric properties from hyper and multispectral imagery with the FLAASH atmospheric correction algorithm,” in *Remote sensing of clouds and the atmosphere X*. Eds. K. Schäfer, A. T. Comerón, J. R. Slusser, R. H. Picard, M. R. Carleer and N. Sifakis (Bruges, Belgium: SPIE Press), 114–124. doi: 10.1117/12.626526
- Richardson, K., Markager, S., Buch, E., Lassen, M. F., and Kristensen, A. S. (2005). Seasonal distribution of primary production, phytoplankton biomass and size distribution in the Greenland Sea. *Deep Sea Res. Part I Oceanogr. Res. Pap.* 52, 979–999. doi: 10.1016/j.dsr.2004.12.005
- Ritchie, R. J. (2018). Measurement of chlorophylls a and b and bacteriochlorophyll a in organisms from hypereutrophic auxinic waters. *J. Appl. Phycol.* 30, 3075–3087. doi: 10.1007/s10811-018-1431-4
- Sathyendranath, S., Prieur, L., and Morel, A. (1989). A three-component model of ocean colour and its application to remote sensing of phytoplankton pigments in coastal waters. *Int. J. Remote Sens.* 10, 1373–1394. doi: 10.1080/01431168908903974
- Shen, F., Zhou, Y. X., Li, D. J., Zhu, W. J., and Salama, M. S. (2010). Medium resolution imaging spectrometer (MERIS) estimation of chlorophyll-a concentration in the turbid sediment-laden waters of the changjiang (Yangtze) estuary. *Int. J. Remote Sens.* 31, 4635–4650. doi: 10.1080/01431161.2010.485216
- Simon, N. S. (1989). Nitrogen cycling between sediment and the shallow-water column in the transition zone of the potomac river and estuary. II. the role of wind-driven resuspension and adsorbed ammonium. *Estuar. Coast. Shelf Sci.* 28, 531–547. doi: 10.1016/0272-7714(89)90028-0
- Sun, L. F., Chang, K. E., Zhaoli, X. U., Que, J. L., and Tian, F. G. (2013). The influence of upwelling and water mass on the ecological group distribution of zooplankton in zhejiang coastal waters. *Acta Ecol. Sin.* 33, 1811–1821. doi: 10.5846/stxb201203090320

- Tao, F., Zhang, Y., Wang, J. J., and Zhang, Y. (2007). Study on quantitative remote sensing models for measuring suspended sediment concentration. *Ocean Engineering* 25, 96–101. doi: 10.1016/S1001-6058(07)60030-4
- Tebbs, E. J., Remedios, J. J., and Harper, D. M. (2013). Remote sensing of chlorophyll-a as a measure of cyanobacterial biomass in lake bogoria, a hypertrophic, saline-alkaline, flamingo lake, using landsat ETM+. *Remote Sens. Environ.* 135, 92–106. doi: 10.1016/j.rse.2013.03.024
- Thomson, R. E., Gower, J. F. R., and Bowker, N. W. (2009). Vortex streets in the wake of the Aleutian islands. *Monthly Weather Review*. 105, 873. doi: 10.1175/1520-0493(1977)105<0873:VSITWO>2.0.CO;2
- Tilstone, G. H., Angel-Benavides, I. M., Pradhan, Y., Shutler, J. D., Groom, S., and Sathyendranath, S. (2011). An assessment of chlorophyll-a algorithms available for SeaWiFS in coastal and open areas of the bay of Bengal and Arabian Sea. *Remote Sens. Environ.* 115, 2277–2291. doi: 10.1016/j.rse.2011.04.028
- Tzortziou, M., Subramaniam, A., Herman, J. R., Gallegos, C. L., Neale, P. J., and Harding, L. W. (2007). Remote sensing reflectance and inherent optical properties in the mid Chesapeake bay. *Estuar. Coast. Shelf Sci.* 72, 16–32. doi: 10.1016/j.eccs.2006.09.018
- Wang, Y. Z., Liu, G., Xue, B., Guo, L., and Zhang, X. L. (2021). "Evaluation of fusion methods for GF-6 aiming to water body observation," in *2021 3rd international conference on geoscience and environmental chemistry* (United Kingdom: EDP Sciences Press), 2–9. doi: 10.1051/e3sconf/202129002009
- Wang, X. L., Wang, B. D., Zhang, C. S., Shi, X. Y., Zhu, C. J., Xie, L. P., et al. (2008). Nutrient composition and distributions in coastal waters impacted by the changjiang plume. *Acta Oceanol. Sin.* 27, 111–125. doi: 10.13140/2.1.3884.6080
- Wolanski, E., and Hamner, W. M. (1988). Topographically controlled fronts in the ocean and their biological influence. *Science* 241, 177–181. doi: 10.1126/science.241.4862.177
- Xia, T., He, Z., Cai, Z. W., Wang, C., Wang, W. J., Wang, J. Y., et al. (2022). Exploring the potential of Chinese GF-6 images for crop mapping in regions with complex agricultural landscapes. *Int. J. Appl. Earth Obs. Geoinf.* 107, 102702. doi: 10.1016/j.jag.2022.102702
- Xu, Y., Nieto, K., Teo, S. L. H., McClatchie, S., and Holmes, J. (2017). Influence of fronts on the spatial distribution of albacore tuna (*Thunnus alalunga*) in the northeast pacific over the past 30 years 1982-2011). *Prog. Oceanogr.* 150, 72–78. doi: 10.1016/j.pocean.2015.04.013
- Xu, L. J., Yang, D. Z., Greenwood, J., Feng, X. R., Gao, G. D., Qi, J. F., et al. (2020). Riverine and oceanic nutrients govern different algal bloom domain near the changjiang estuary in summer. *J. Geophys. Res. Biogeosci.* 125, e2020JG005727. doi: 10.1029/2020JG005727
- Yang, A., Zhong, B., Hu, L., Wu, S., Xu, Z., Wu, H., et al. (2020). Radiometric cross-calibration of the wide field view camera onboard GaoFen-6 in multispectral bands. *Remote Sens.* 12, 1037. doi: 10.3390/rs12061037
- Zawadzki, J., and Kedzior, M. (2016). Soil moisture variability over odra watershed: comparison between SMOS and GLDAS data. *Int. J. Appl. Earth Obs. Geoinf.* 45, 110–124. doi: 10.1016/j.jag.2015.03.005
- Zhai, Z. K., Lu, S. L., Wang, P., Wang, C., Tang, H. L., Liu, D. Y., et al. (2021). "Ocean chlorophyll-a retrieval using GF1-WFV data-a case study of the central bohai sea," in *The 2nd international conference on advances in civil and ecological engineering research* (USA: IOP Press), 12–21. doi: 10.1088/1755-1315/626/1/012021
- Zhou, Y. D., and Li, S. F. (2018). "the main economic species in East China Sea three channels," in *The main economic species in East China Sea three channels and a protection zone atlas*. Eds. C. G. Yu, K. D. Xu and H. L. Zhang (Beijing China: China Ocean Press), 44–69.
- Zhu, J. P., Hu, H. M., Gu, B. Q., Yu, B. C., Li, T. J., Zhang, Y. Y., et al. (2014). The content of chlorophyll a in Dongji Islands Sea area and its correlation analysis with environmental factors. *J. Zhejiang Ocean Univ. (Nat. Sci.). In Chin.* 33, 257–261, 271.
- Zhu, W., Pang, S., Chen, J., Sun, N., Huang, L., Zhang, Y., et al. (2020). Spatiotemporal variations of total suspended matter in complex archipelagic regions using a sigmoid model and landsat-8 imagery. *Reg. Stud. Mar. Sci.* 36, 101308. doi: 10.1016/j.rsma.2020.101308
- Zhu, W. N., Yu, Q., Tian, Y. Q., and Becker, B. L. (2015). Issues and potential improvement of multiband models for remotely estimating chlorophyll-a in complex inland waters. *IEEE J. Selected Topics Appl. Earth Observations Remote Sensing.* 8, 562–575. doi: 10.1109/JSTARS.2014.2360872